

Teleseismic Body Waves from Dynamically Rupturing Shallow Thrust Faults: Are They Opaque for Surface-Reflected Phases?

by Deborah Elaine Smith, Brad T. Aagaard, and Thomas H. Heaton

Abstract We investigate whether a shallow-dipping thrust fault is prone to wave-slip interactions via surface-reflected waves affecting the dynamic slip. If so, can these interactions create faults that are opaque to radiated energy? Furthermore, in this case of a shallow-dipping thrust fault, can incorrectly assuming a transparent fault while using dislocation theory lead to underestimates of seismic moment?

Slip time histories are generated in three-dimensional dynamic rupture simulations while allowing for varying degrees of wave-slip interaction controlled by fault-friction models. Based on the slip time histories, P and SH seismograms are calculated for stations at teleseismic distances. The overburdening pressure caused by gravity eliminates mode I opening except at the tip of the fault near the surface; hence, mode I opening has no effect on the teleseismic signal. Normalizing by a Haskell-like traditional kinematic rupture, we find teleseismic peak-to-peak displacement amplitudes are approximately 1.0 for both P and SH waves, except for the unrealistic case of zero sliding friction. Zero sliding friction has peak-to-peak amplitudes of 1.6 for P and 2.0 for SH waves; the fault slip oscillates about its equilibrium value, resulting in a large nonzero (0.08 Hz) spectral peak not seen in other ruptures. These results indicate wave-slip interactions associated with surface-reflected phases in real earthquakes should have little to no effect on teleseismic motions. Thus, Haskell-like kinematic dislocation theory (transparent fault conditions) can be safely used to simulate teleseismic waveforms in the Earth.

Definition of Terms

To avoid confusion about terminology we first wish to clearly define how we will be using the following terms. When we refer to other articles that may have different definitions, we will enclose them in quotes.

1. *Dislocation theory*. Application of shear double couples to approximate a jump in displacement across a fault surface. There is no true cut in the medium; the double couples simply stretch the elastic medium to create high strains across an infinitesimally thin zone.
2. *Haskell-like rupture*. It can be applied to either a dislocation or a true cut boundary. Traditionally, it is a propagating pulse of slip where slip at any point is a ramp function in time. There is no reslipping.
3. *Dynamic rupture*. A finite-element model with a true cut (fault) and specified tractions or slips. Reslipping may or may not occur, depending on the evolution of the dynamic rupture simulation.

Introduction

It has been suggested that “dislocation” models may seriously underestimate seismic energy for shallow-angle

thrust events (Brune, 1996; Shi *et al.*, 1998). It is hypothesized that seismic energy may be partially trapped in the hanging wall during shallow-angle thrust events; hence, teleseismic measurements would measure only some fraction of the total signal. This idea springs, in part, from reported discrepancies between near-field (regional) and far-field (teleseismic) measurements of radiated energy where the near-field estimates have sometimes far exceeded the far-field estimates (Shoja-Taheri and Anderson, 1988; Sing and Ordaz, 1994). Although this reported discrepancy was resolved for the strike-slip Hector Mine earthquake (Boatwright *et al.*, 2002), it remains to be seen if it can be resolved for shallow, thrust-fault events. The suggestion that energy may be trapped in the hanging wall of shallow, thrust-fault events raises concerns regarding a transparent fault boundary condition when using “dislocation” theory to model earthquake sources. A transparent fault boundary is a rupture plane that allows seismic energy to pass through unimpeded; as a result, there is no interaction between the earthquake rupture and the seismic phases (which reflect off the Earth’s surface and then propagate back down through a dipping rupture) in terms of reslipping. Reslipping is where radiated

waves from the main slipping episode cause additional slip on the same rupture interface. In contrast, for a fault boundary with wave-slip interactions that produce reslipping, the surface-reflected phases (e.g., pP , sP , sS) interact with the rupture, potentially trapping energy in the overhanging wedge of a thrust fault. So we ask, do wave-slip interactions on a shallow-dipping thrust fault result in a fault surface that is opaque to radiated energy, leading to reduced telesismic ground motions? If earthquakes do indeed have opaque fault boundaries that decrease the telesismic ground motions and if scientists do not take this effect into account (i.e., they assume a transparent fault for traditional Haskell-like dislocation modeling of telesismic data), then scientists could possibly underestimate the seismic energy released and the seismic moment.

At telesismic distances, most of the radiated energy is low-frequency energy (<1 Hz), where the zero-frequency component equals the moment. In practice, seismic moment is more often used to estimate the size of earthquakes from telesismic waveforms; therefore, in this study of telesismic ground motions we will address the concern about Haskell-like dislocation theory in the context of seismic moment.

In a series of foam-rubber block experiments intended to simulate earthquake ruptures, Brune (1996) observed significant mode I motion (opening) in addition to shear (mode II and mode III) displacements. The mode I opening resulted in considerable wave-slip interactions and an opaque boundary that trapped radiated energy in the overhanging wedge. Figure 1 schematically shows what such an opaque boundary might look like for a dip-slip fault. Other work that has also seen significant mode I opening are the more realistic 2D lattice models of Shi *et al.* (1998). Brune (1996) suggested that if modeling of earthquakes took into account this hypothesized opaque boundary, reported discrepancies between near-field and far-field radiation estimates might be resolved. In particular, near-field estimates of radiated energy for thrust faults have often greatly exceeded the far-field (telesismic) estimates (Shoja-Taheri and Anderson, 1988; Boatwright *et al.*, 2002). Also the near-field estimates of apparent stress, that is, seismic energy divided by moment, can exceed the far-field estimates of apparent stress (Sing and Ordaz, 1994); Brune hypothesizes this is caused by an opaque boundary trapping the radiated energy close to the fault.

Hence, we investigate whether ruptures on a shallow-dipping thrust fault actually produce fault boundary opacity (mode I opening and mode II/mode III shear displacement opacity) and reduce telesismic signals by examining telesismic P and SH body waves. Using dynamic rupture simulations, we generate earthquake ruptures while allowing different levels of wave-slip interactions. We found that realistic overburdening pressure eliminates mode I opening in the ruptures except at the very shallow surface (see Discussion for more details). We then compute telesismic body waves by using these simulated earthquake ruptures. If wave-slip interactions produce fault boundaries that are

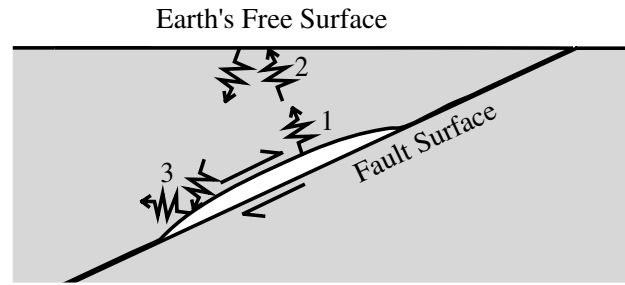


Figure 1. Cartoon illustrating how an earthquake rupture might make a fault appear opaque to propagating waves: (1) seismic energy radiated from rupture, (2) energy reflects off of free surface, and (3) energy reflects off opaque fault boundary, trapping energy in the overhanging wedge.

opaque to telesismic waves, then one might expect ruptures with the greatest interactions to generate the smallest-amplitude telesismic motions.

Methodology

We compute synthetic telesismic P and SH body waves in a two-step process shown in Figure 2. We generate slip time histories using 3D finite-element dynamic rupture simulations and then calculate the telesismic waveforms corresponding to these slip time histories with the method of Yao and Ji (1997) and Yao and Harkrider (1983). We can map finite-element solutions into point-dislocation time histories to compute telesismic distances, because in an elastic space, either a stress boundary condition on a sliding surface (like our finite-element dynamic ruptures) or a displacement boundary condition on a box bounding the sliding surface (like our telesismic computations) uniquely determines the solution (Achenbach, 1973, section 3.2). We will refer to the stress boundary condition as a dynamic representation and the displacement boundary condition as a dislocation representation.

In our dynamic ruptures, the friction model, the elastodynamic equations, and an initial stress state determine the stress on the sliding surface, $\tau(X_1, X_2, X_3 = 0, t)$, and from this we can calculate the displacement jump, $D(X_1, X_2, t)$, across the surface of the fault (Fig. 3). The dislocation representation, which we use for our forward calculations of telesismic ground motions, begins with specifying the displacement jump, $D'(X_1, X_2, t)$, across the surface of the fault. If we equate $D(X_1, X_2, t)$ to $D'(X_1, X_2, t)$, then our dislocation representation (used to calculate our telesismic ground motions) has an identical elastodynamic field as the finite-element dynamic rupture simulation. In other words, the two representations, dynamic and dislocation, produce the same stresses and displacements everywhere, except inside an infinitesimally thin box bounding the fault. Because we map the irregularly spaced dynamic rupture time histories into a coarser, regularly spaced grid of dislocation time histories,

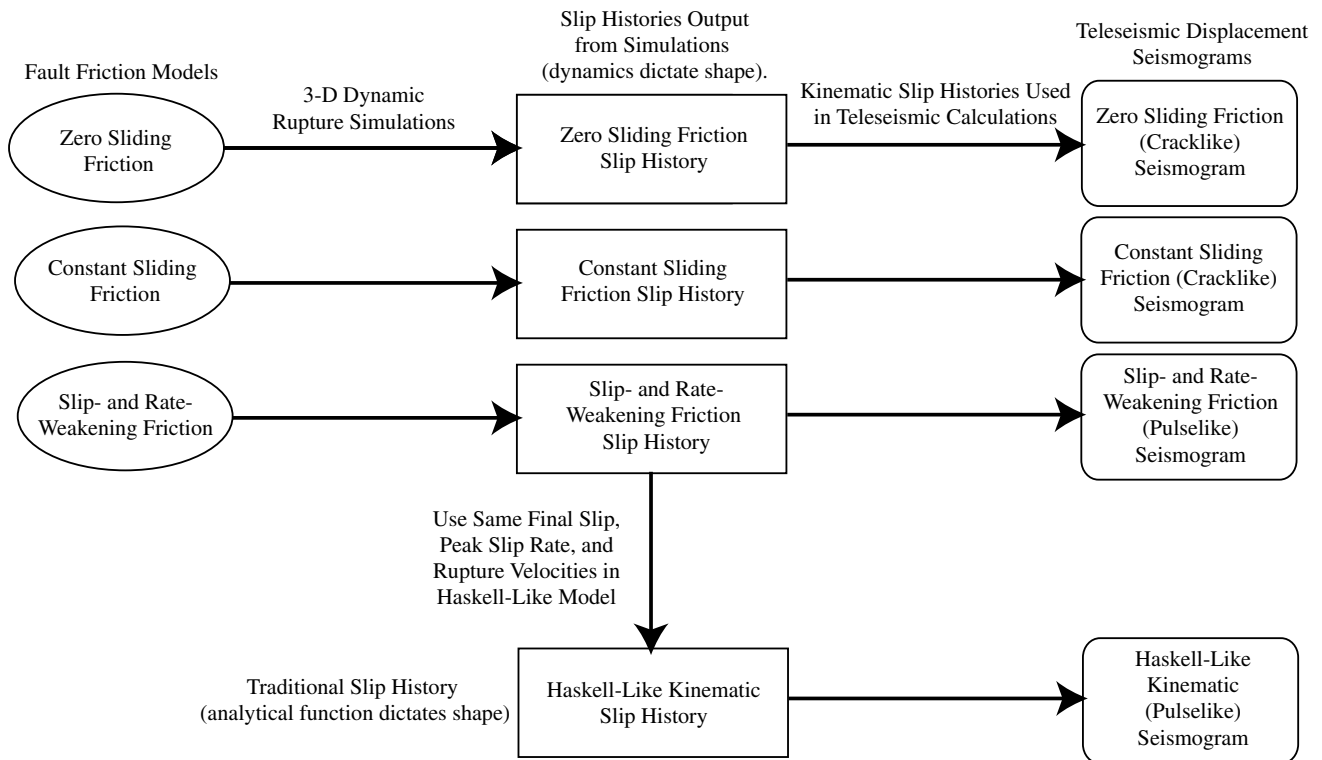


Figure 2. Flowchart showing how the teleseismic seismograms for the four models are made. For the three dynamic models, we start with frictional constitutive laws used in the 3D dynamic rupture simulations: (1) zero sliding friction, (2) constant sliding friction, and (3) slip- and rate-weakening friction. The 3D dynamic rupture simulations produce slip histories. The resultant slip histories are kinematic descriptions of slip on the fault during rupture. Yet at the same time, they account for dynamic effects by expressing reslipping episodes or other modifications to their shape. In addition to the three slip histories that are a result of our dynamic rupture simulations we also produce analytically a traditional Haskell-like slip history. The Haskell-like slip history is designed to have parameters similar to the slip- and rate-weakening friction model, but without reslipping. Hence, the traditional kinematic Haskell-like model slip history should be completely transparent to reflected seismic energy. Then we take all four kinematic slip histories and use them as input for teleseismic calculations to produce our resultant displacement seismograms as seen in the Results section.

the two solutions are not exactly the same close to the fault. However, the two solutions converge far away from the fault so the teleseismic results for the two representations are equivalent. This allows us to compute the teleseismic body waves for the different degrees of wave-slip interactions associated with different friction models.

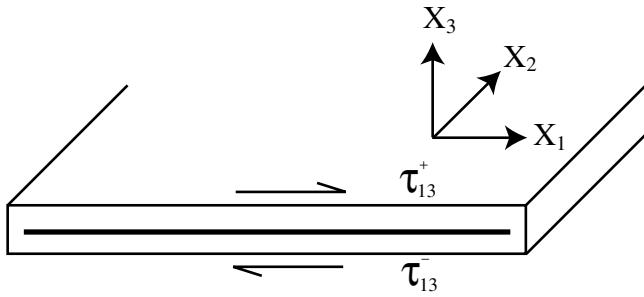
The unique aspect of this approach is that it takes advantage of the strengths and avoids the weaknesses of each modeling method. Strengths include the following: (1) Dynamic rupture simulations incorporate full fault dynamics, friction, fracture energy, radiated waves, etc., enabling us to explicitly account for wave-slip interactions, and (2) dislocation theory has a rich analytical background that has paved the way for fast and accurate computation of teleseismic signals. Weaknesses that we avoid include the following: (1) It is not feasible to construct a dynamic rupture grid that has a sufficiently large number of elements to calculate both the dynamic motions on a sliding fault and the teleseismic

body wave for periods down to 2 sec, and (2) dislocation theory is purely kinematic and cannot explicitly incorporate fault physics.

Dynamic Rupture Modeling

Calculation Method

The solution techniques for solving our dynamic earthquake ruptures in finite-element simulations have been discussed in a few articles (Aagaard, 1999; Aagaard *et al.*, 2001). The dynamic elasticity equation is solved within a three-dimensional domain discretized with linear tetrahedral elements. Friction models control the evolution of the stress field under the constraint that friction produces reasonable rupture dynamics. See Aagaard *et al.* (2001) for more detail regarding the constraints on the friction model. The resulting earthquake ruptures have realistic depth distributions of slip,



Net traction across surface boundary = 0.
Specifically, $\tau_{13}^+ = \tau_{13}^-$.

Figure 3. Comparison of dislocation versus dynamic representations. In the dynamic representation (1) we compute the stress boundary condition on an actively slipping fault, $\tau(X_1, X_2, X_3 = 0, t)$, that is compatible with friction models, elastodynamic equations, and the assumed initial stress. (2) From $\tau(X_1, X_2, X_3 = 0, t)$, we can calculate the displacement on either side of the fault, $u^+(X_1, X_2, X_3 = +0, t)$ and $u^-(X_1, X_2, X_3 = -0, t)$. (3) This determines the displacement jump, $D(X_1, X_2, t)$, where $D(X_1, X_2, t) = u^+(X_1, X_2, X_3 = +0, t) - u^-(X_1, X_2, X_3 = -0, t)$. (3) From $D(X_1, X_2, t)$, we can compute $\tau(X_1, X_2, X_3, t)$ everywhere in the media. In the dislocation representation, (1) we specify a displacement jump, $D'(X_1, X_2, t)$, across the width of an infinitesimally thin, linearly elastic box enclosing the fault. We do this by applying a singular body force that stretches the linear elastic material within the box, a finite amount, $D'(X_1, X_2, t)$, over the infinitesimal box width. (2) We can calculate the stress caused by this displacement jump, $\tau'(X_1, X_2, X_3, t)$, everywhere. If $D(X_1, X_2, t) = D'(X_1, X_2, t)$, then $\tau(X_1, X_2, X_3, t) = \tau'(X_1, X_2, X_3, t)$ by the uniqueness theorem (Achenbach, 1973, section 3.2), including $\tau_{13}^+ = \tau_{13}^- = \tau_{13}^{\prime+} = \tau_{13}^{\prime-}$. That is, the dynamic and kinematic solutions are mathematically identical everywhere except inside an infinitesimally thin box surrounding the rupture. Inside this box, the solutions are inherently different. For the dynamic representation there is a cut in the material, whereas in the dislocation representation, there is a singular body force that stretches the elastic material. But again, the solutions are identical outside the infinitesimally thin box surrounding the linearly elastic material; hence, when comparing the two representations one must “think outside the box.”

rupture velocities, average final slip, and peak particle velocities.

A shallow thrust-fault plane that breaks the surface with a 23° dip is placed in the middle of the simulation domain as shown in Figure 4. Earthquakes on this fault plane have a nominal rake angle of 90° for all the ruptures. In each case, the hypocenter is located midway (14 km) along-strike and 13 km down-dip. Material properties vary as a function of depth in a piecewise linear fashion as illustrated in Figure 5. Going from deeper to shallower, the major change in material properties occurs at approximately 6 km depth where the velocities and density steeply decrease to simulate soft-basin structure. The spatial resolution, 170 m at surface and 660 m at 7 km depth, yields a 2-sec lower bound on the period of the radiated waves.

The dynamic ruptures can be divided into two classes based on the type of friction model that controls the evolution of the stress field. The first class includes cracklike ruptures that are controlled by slip-weakening friction. Slip weakening has a long history of being used to study frictional sliding in earthquakes, including Ida (1972), Andrews (1976a), and Burridge *et al.* (1979). Sliding friction drops to a nominal value after slip progresses to some amount D_0 as shown in Figure 6. Note that the slip-weakening parameter, $D_0 = 2E_G/(\sigma_{\max} - \sigma_{\min})$, where E_G is the fracture energy, σ_{\max} is the maximum frictional stress, and σ_{\min} is the minimum frictional stress. The ruptures with slip-weakening friction are cracklike because healing phases are initiated when the rupture reaches the boundaries of the fault. In one scenario (constant sliding friction), the minimum value of sliding stress is sufficiently larger than zero to arrest slip when healing phases arrive and the shear traction drops below this minimum sliding stress. Note that in this case, when the friction drops to this minimum value, the fault has a constant friction boundary condition, not a constant stress boundary condition. The minimum sliding friction provides an upper limit on the traction magnitude. In another scenario (zero sliding friction), the final minimum sliding stress is zero, creating a traction-free sliding surface, which allows the fault slip to overshoot and then oscillate about its equilibrium position.

The second class of dynamic ruptures includes pulslike

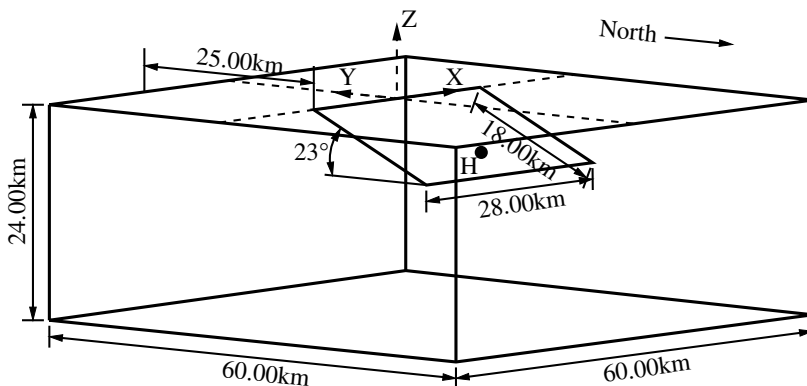


Figure 4. Geometry of the shallow-thrust fault that breaks the surface of the finite-element grid. It has a rake of 90° . The hypocenter, H , is located 14 km along-strike and 13 km down-dip.

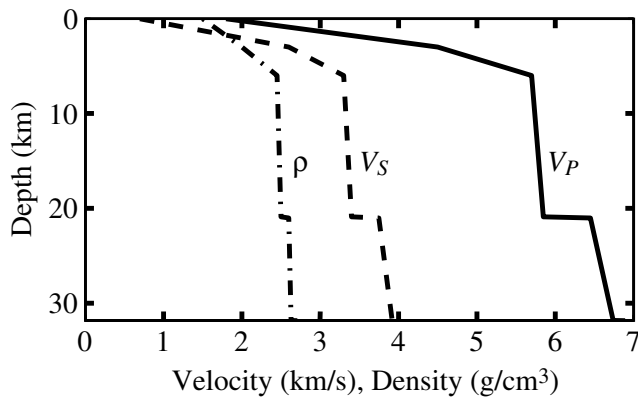


Figure 5. Material properties as a function of depth for the source region. The symbols represent the following: ρ is density, V_S is S -wave velocity, and V_P is P -wave velocity. The values decrease close to the surface to simulate basin structure.

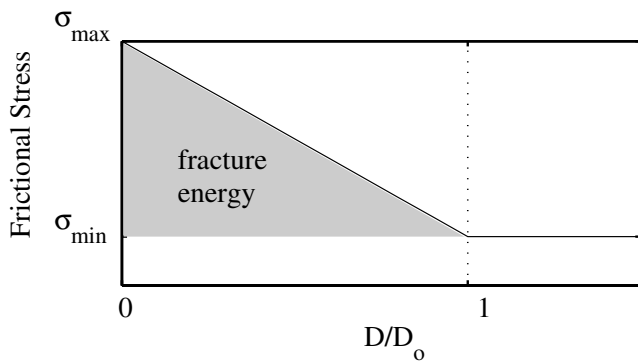


Figure 6. A slip-weakening friction model. The frictional stress reduces from maximum to a minimum value as slip increases to D_0 . The shaded region is associated with the fracture energy.

ruptures that are controlled by slip- and rate-weakening friction. The slip- and rate-weakening applied here is based on the models of Madariaga and Cochard (1996) and Madariaga *et al.* (1998). Shear stress initially drops as slip occurs and then rises as the slip rate drops below a given threshold, V_0 , as shown in Figure 7. In this case, $\sigma_{\text{post}} - \sigma_{\text{min}} = 2/3 (\sigma_{\text{max}} - \sigma_{\text{min}})$, where σ_{post} is the final frictional stress, and $V_0 = 0.10$ m/sec. The ruptures with slip- and rate-weakening friction are pulselike because the healing phases occur spontaneously and trail behind the leading edges of the rupture, producing much narrower actively slipping regions than the cracklike ruptures (Heaton, 1990). A more detailed description of the friction models can be found in Aagaard *et al.* (2001).

In Table 1 frictional stress values and fracture energy values are given at three depths, 0 km, 3 km, and 6 km. They vary linearly between the depths of 0–3 km, linearly between the depths of 3–6 km, and are uniform below 6 km depth. The sliding stress is what we have termed σ_{min} and the failure

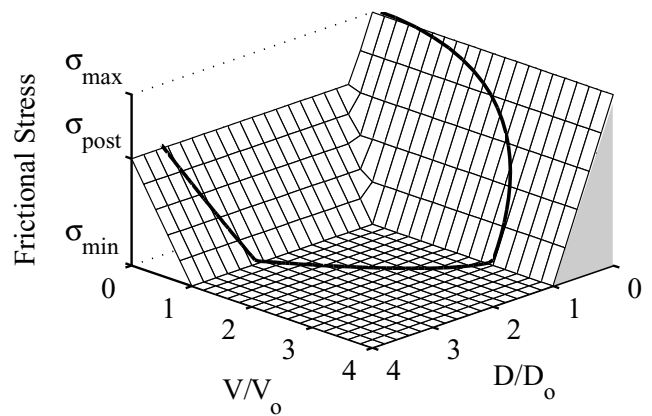


Figure 7. A slip- and rate-weakening model. The dark line represents a typical trajectory as a function of time of the frictional stress for a point on the fault. At first frictional stress decreases with increasing slip up to a critical slip, D_0 . Then frictional stress increases as velocity falls below a critical velocity, V_0 .

Table 1
The Variation as a Function of Depth of Initial Shear Stress, Shear Stress at Failure, Shear Stress due to Frictional Sliding during Rupture, and Fracture Energy for the Four Models

	Depth (km)	Sliding Stress (MPa)	Failure Stress (MPa)	Fracture Energy (MJ/m ²)	Initial Stress (MPa)
Zero sliding friction (cracklike)	0.0	0.00	0.75	0.18	0.11
	3.0	0.00	3.04	0.80	2.05
	6.0+	0.00	7.65	1.50	4.05
Constant sliding friction (cracklike)	0.0	0.25	1.00	0.18	0.14
	3.0	1.00	4.04	0.80	2.51
	6.0+	1.00	8.65	1.50	4.95
Slip- and rate-weakening friction (pulselike)	0.0	0.50	1.00	0.12	0.19
	3.0	1.00	5.76	1.80	3.42
	6.0+	1.00	12.00	2.89	6.75

The values vary approximately linearly between 0 and 3 km depth, linearly between 3 and 6 km depth, and are uniform below 6 km depth. Initial shear stress and shear stress at failure increase with depth because of the increasing overburdening pressure of the rock. Initial shear stress is less than the shear stress at failure; therefore, a stress asperity is needed to start the rupture. We vary the stress drop with depth to produce distributions of slip without a clear depth dependence.

stress is what we have termed σ_{max} . Last, there are differences in the stress and fracture energies in each friction model in an attempt to produce similar source parameters (final slip and average rupture speed) for the dynamic ruptures. Varying stress controls the final slip, and varying fracture energy controls the average rupture speed.

In these formulations of the slip-weakening and slip- and rate-weakening friction models, we assume that the physical processes controlling the changes in stress on the fault during sliding yields a friction stress that is independent of the normal stress. However, when we allow fault opening, the friction stress does go to zero when the fault has zero

normal stress. Although traditional friction model formulations in dynamic rupture simulations use a coefficient of friction to allow dynamics variations in normal stresses to influence the friction stress, they do not include normal stresses that increase with depth corresponding to the overburden pressures. Because the overburden pressure over most of the fault is about two orders of magnitude greater than dynamic normal stress changes during the rupture, dynamic normal stress changes would not significantly alter the frictional sliding stresses, except very close to the ground surface. In other words, if we reformulated our friction models using a coefficient of friction, dynamic normal stress changes that are small compared with the overburden pressure would result in correspondingly small changes to the friction stress. At seismogenic depths these stress changes would be negligible, so we chose not to include them.

Our traditional kinematic rupture is also pulselike and has slip similar to traditional Haskell models (Haskell, 1964), hence, the Haskell-like label. Using a slip time history that follows the integral of Brune's (1970) far-field time function, the Haskell-like traditional kinematic rupture is constructed to approximately match only the pulselike slip- and rate-weakening friction model (Fig. 2). When (1) the final slip and slip onset times (rupture velocities) are matched between the Haskell-like traditional kinematic rupture and the slip- and rate-weakening friction rupture and (2) the rise times of the Haskell-like traditional kinematic rupture are set to match the peak slip rates in the dynamic slip- and rate-weakening friction rupture, then the only difference between the two ruptures is the shape of their slip time histories. It is the shape of their respective time histories that will produce dissimilar wave-slip interactions, where the Haskell-like traditional kinematic rupture is transparent (shape is fixed a priori, and there are no wave-slip interactions) and the slip- and rate-weakening rupture allows wave-slip interactions.

Zero sliding friction allows the most wave-slip interactions because it allows for complete shear-traction decoupling once the critical, D_0 , is achieved. Constant sliding friction permits the second most wave-slip interactions. The dynamic rupture allowing the least wave-slip interactions is the pulselike slip- and rate-weakening friction. Last, the Haskell-like traditional kinematic rupture is completely transparent (no interactions) by construction.

These friction models (cracklike constant sliding friction, cracklike zero sliding friction, and pulselike slip- and rate-weakening friction) control the development of the stress field and the rupture dynamics while an earthquake is underway. A uniform strain field provides the driving force for the earthquake rupture. This produces slip with no systematic depth dependence, which is compatible with kinematic source inversions (Heaton, 1990; Somerville *et al.*, 1999). This is in contrast with the assumptions of constant static stress drop, or constant dynamic stress drop, both of which would produce large systematic variations in slip with depth in our layered half-space. Using the coordinate system

in Figure 4, we apply the following tectonic strain field, ϵ^t , to simulate tectonic strain:

$$\begin{aligned} \epsilon_{yy}^t &= -C \\ \epsilon_{xx}^t &= \epsilon_{zz}^t = -V\epsilon_{yy}^t \\ \epsilon_{xy}^t &= \epsilon_{yz}^t = \epsilon_{xz}^t = 0, \end{aligned} \quad (1)$$

where V is Poisson's ratio and C is a constant. The values of C are:

$$C = \begin{cases} 1.69 \times 10^{-4} & \text{for zero sliding friction (cracklike)} \\ 2.06 \times 10^{-4} & \text{for constant sliding friction (cracklike)} \\ 2.81 \times 10^{-4} & \text{for slip- and rate-weakening friction (pulselike)}. \end{cases}$$

Note, different values of C are associated with different levels of shear stress to create similar final slips among the three models. We also include the overburden pressure,

$$\begin{aligned} \epsilon_{xx}^g &= \epsilon_{yy}^g = \epsilon_{zz}^g = \frac{1}{3\lambda + 2\mu} \int_0^z \rho(s)g ds \\ \epsilon_{xy}^g &= \epsilon_{yz}^g = \epsilon_{xz}^g = 0. \end{aligned} \quad (2)$$

The strain fields given in (1) and (2) produce both normal and shear tractions on the fault interface. The shear tractions are in the direction of desired slip and are the driving stress for the earthquake rupture. Initially, they are somewhat below the failure level (Table 1), but after the rupture starts, the concentration of shear stress ahead of the leading edge of the rupture increases the total shear stress above the failure level. A circular stress asperity (an area of high-shear tractions, 2% larger than the failure stress) of radius 2 km, located at the desired hypocenter, initiates the rupture. The earthquake starts at the asperity, spreads out in an elliptical fashion over the rest of the fault, and then arrests at the boundaries of the fault. The fault boundaries, which determine the spatial extent of the earthquake, are created by tapering the initial shear traction to a small value. Figure 8 shows the spatial distribution of the initial fault traction, including the stress asperity and tapered edges. Table 1 gives the control points for the nominal depth dependence of the initial shear stress.

Slip History Results

We aim for similar source parameters in the dynamic ruptures, but small differences exist in the final slip, rupture velocities, and peak slip velocities. Consequently, we scale the slip histories so that all four scenarios have a seismic potency of $P = 4.68 \times 10^8 \text{ m}^3$, where $P = \bar{D}A$, \bar{D} is average slip and A is area (Heaton and Heaton, 1989; Ben-Zion and Zhu, 2002). By design, the traditional Haskell-like kinematic model shares the same slip rate and slip onset times (rupture velocities) as those in the slip and rate-weakening friction rupture. Table 2 summarizes the slip-history information of the four ruptures.

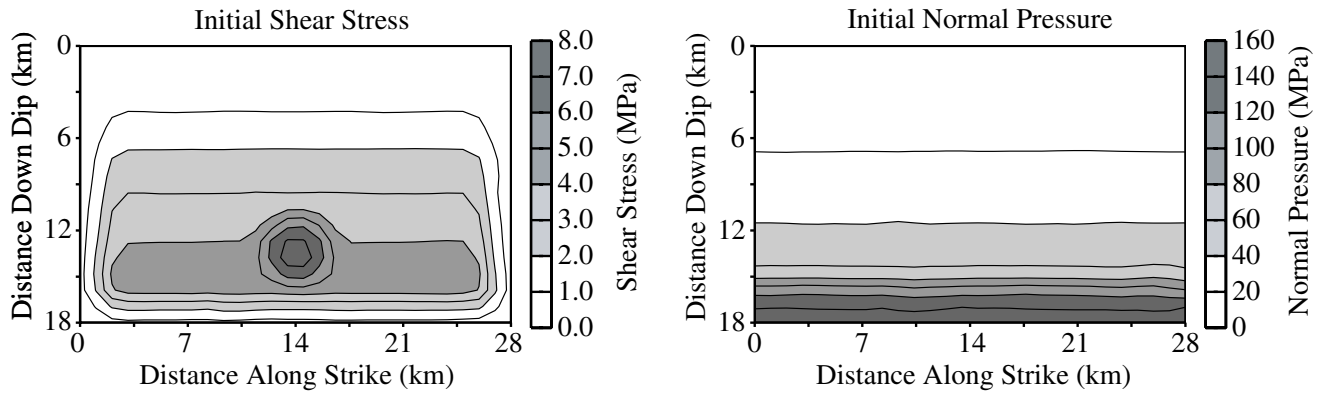


Figure 8. Schematic illustration of the initial shear tractions and normal pressures on the thrust fault. The increase in normal pressure as a function of depth is caused by the overburden pressure. The shear traction has an asperity of higher stress to initiate the earthquake and edges tapered to a lower stress to keep the rupture confined within a predetermined boundary.

Table 2

The Slip History (Average Final Slip and Maximum Final Slip), Slip-Rate History (Average Peak Slip Rate and Maximum Peak Slip Rate), and Potency Statistics for the Four Models

	Final Slip		Peak Slip Rate		Potency (m^3)
	Avg. (m)	Max. (m)	Avg. (m/sec)	Max. (m/sec)	
Zero sliding friction (cracklike)	0.94	1.62	0.47	2.22	4.68×10^8
Constant sliding friction (cracklike)	0.94	1.47	0.37	2.02	4.68×10^8
Slip- and rate-weakening friction (pulselike)	1.00	2.13	0.65	2.79	4.68×10^8
Slip- and rate-weakening friction with opening (pulselike)	1.00	2.06	0.65	2.87	4.68×10^8
Haskell-like kinematic (pulselike)	1.00	2.14	0.65	2.74	4.68×10^8

Note that the source parameters for slip- and rate-weakening friction and the Haskell-like model closely match. The very slight differences between these two pulselike models arises from the interpolation between the grids; the slip and peak slip rate distributions are almost exactly the same. The parameters have been normalized such that the potencies are all, $P = 4.68 \times 10^8 \text{ m}^3$.

In preparation for our teleseismic calculations, we interpolate the slip histories from dynamic rupture models (nonuniform grid) to a grid of 18×28 points (uniform grid), and low-pass filter the time histories using a fourth order Butterworth filter with a corner frequency of 0.5 Hz. Because most of the radiated energy is at periods longer than 2.0 sec, this removes only a little energy near the high-frequency limit of the simulations and slightly reduces the peak slip rates. For example, the cracklike average peak slip rates are reduced by 1–6%, and the pulselike average peak slip rates are reduced by 10–25%.

To visualize the down-dip and along-strike variations, we plot the slip time histories for a series of points in two cross sections, AA', which runs down the dip of the fault, and BB', which runs along the strike of the fault. Figure 9 shows the locations of these two cross sections, and Figure

10 shows the slip time histories along the cross-sections. Slip parallel to the strike is minimal for all points on the fault, except in the case of zero sliding friction. For zero sliding friction, the fault oscillates symmetrically about AA', and there is significant strike-parallel slip for points on either side of AA'.

Rupture in the mode II direction (the direction of the AA' profile) reaches a rupture speed of 63–83% of V_S , where V_S varies as a function of depth depending on the material properties. Despite larger fracture energies over most of the fault, the slip- and rate-weakening friction's mode II rupture is slightly faster than the other dynamic ruptures (constant sliding friction and zero sliding friction) due to the slip- and rate-weakening friction's faster slip rates for comparable slip. Rupture in mode III (the direction of the BB' profile) accelerates rapidly and then approaches a stable speed within

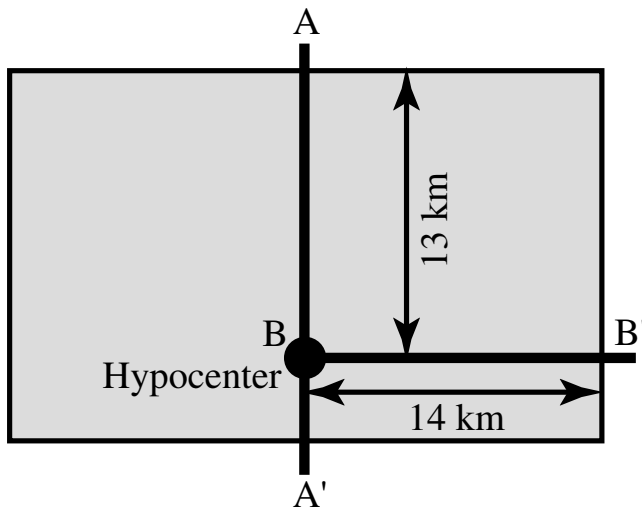


Figure 9. Diagram showing the locations of the two cross sections AA' and BB'. BB' only traverses the right half of the fault because slip is symmetric with respect to the fault's center line.

a few kilometers of the hypocenter. In the absence of fracture energy, mode III rupture should be faster than mode II rupture relative to the shear-wave speed, but in our models fracture energy is included to stabilize the numerical solution. Fracture energy, which slows rupture propagation, affects mode III more strongly than it does mode II (Andrews, 1976b; Day, 1982; Madariaga *et al.*, 1998); as a result, rupture in the mode II direction in our models propagates approximately 20% faster than the mode III rupture.

In the AA' slip time histories, the final slip exhibits a small increase as the rupture approaches the free surface. This is a result of a static effect that is accentuated by dynamics. Static offsets from a constant stress-drop fault in an elastic half-space produces the largest displacements where the fault breaks through to the free surface (Mansinha and Smylie, 1971; Parsons *et al.*, 1988; Okada, 1992; Madariaga, 2003). The fault-rupture dynamics accentuate this trend. At any one instant in time, only a fraction of the fault is slipping. If the entirety of the slipping zone is below the free surface, then the fault rupture at that moment behaves like a buried fault whose slip tapers to zero at the edges. However, as the rupture progresses upward from the hypocenter to the free surface, the slipping zone will eventually include the free surface. When it does, the rupture at that instant in time acts like a fault that breaks through to the free surface where slip is a maximum at the free surface. There is also a difference in the depth distribution of slip between the cracklike and pulselike ruptures. As seen in the AA' slip time histories of Figure 10, the pulselike ruptures have a greater percentage of slip partitioned near the surface and less at depth than the cracklike ruptures. This occurs because the pulselike ruptures have faster slip rates than the cracklike ruptures, which result in more energetic breakout phases at the free surface.

Zero sliding friction overshoots and then oscillates about the final slip along both profiles AA' and BB' because all locations on the fault rupture are oscillating. These oscillations tend to be complex near the surface and more sinusoidal at depth with a period of 12 sec. Additionally, it has multiple modes of oscillation including along-dip and along-strike modes. Because energy cannot be dissipated through frictional sliding, it is dissipated through radiation damping, wherein energy is transferred from the source to the far field as the material oscillates and radiates far-field elastodynamic waves. In this case, the radiation damping of the fundamental mode of zero sliding friction is 6%. Note this is substantially smaller than the radiation damping of 58% for a uniform spherical cavity oscillating radially in a Poissonian whole space (Achenbach, 1973). This difference in radiation damping results from the differences in geometry between a dip-slip fault oscillating about its equilibrium position and the radial oscillation of a uniform cavity. Whereas the behavior of zero sliding friction is highly unrealistic, its teleseismic ground motions are important as our end-member rupture that permits the most wave-slip interactions; hence, if opacity is a problem, zero sliding friction should accentuate its effects.

Figure 10 also shows the long slip durations (up to 14 sec) that occur for the cracklike constant sliding friction rupture. The long-duration slip takes place because healing fronts in the cracklike ruptures initiate only when the rupture reaches one of the fault's boundaries. Then the healing fronts sweep in toward the center of the fault, terminating slip along the way. Therefore, one sees an extended period of slip toward the center and more pulselike slip behavior toward the edges of the fault. Since the ruptures have only a pP reflected phase delay of 3 sec, an sP delay of 4.5 sec, and an sS delay of 6 sec near the hypocenter, we know that the cracklike ruptures, with their long slip intervals, allow for ample interactions between the rupture and radiated seismic waves.

On the other hand, the pulselike ruptures generally have slip durations of less than 5 sec. In the case of slip- and rate-weakening, the healing front spontaneously follows the rupture front in accordance with its friction model. As a result, the width of the rupture at a given point in time is much smaller than what we find in the cracklike ruptures, so the slip duration is shorter. With this shorter slip duration, there is less opportunity for interactions between the rupture and radiated energy; that is, slip- and rate-weakening would have less chance of being opaque than either cracklike rupture. The Haskell-like traditional kinematic rupture is transparent with no interaction by design.

Teleseismic Waveform Modeling

Calculation Method

Using the slip histories as point-dislocation sources distributed on a fault-plane grid in a continuous elastic medium,

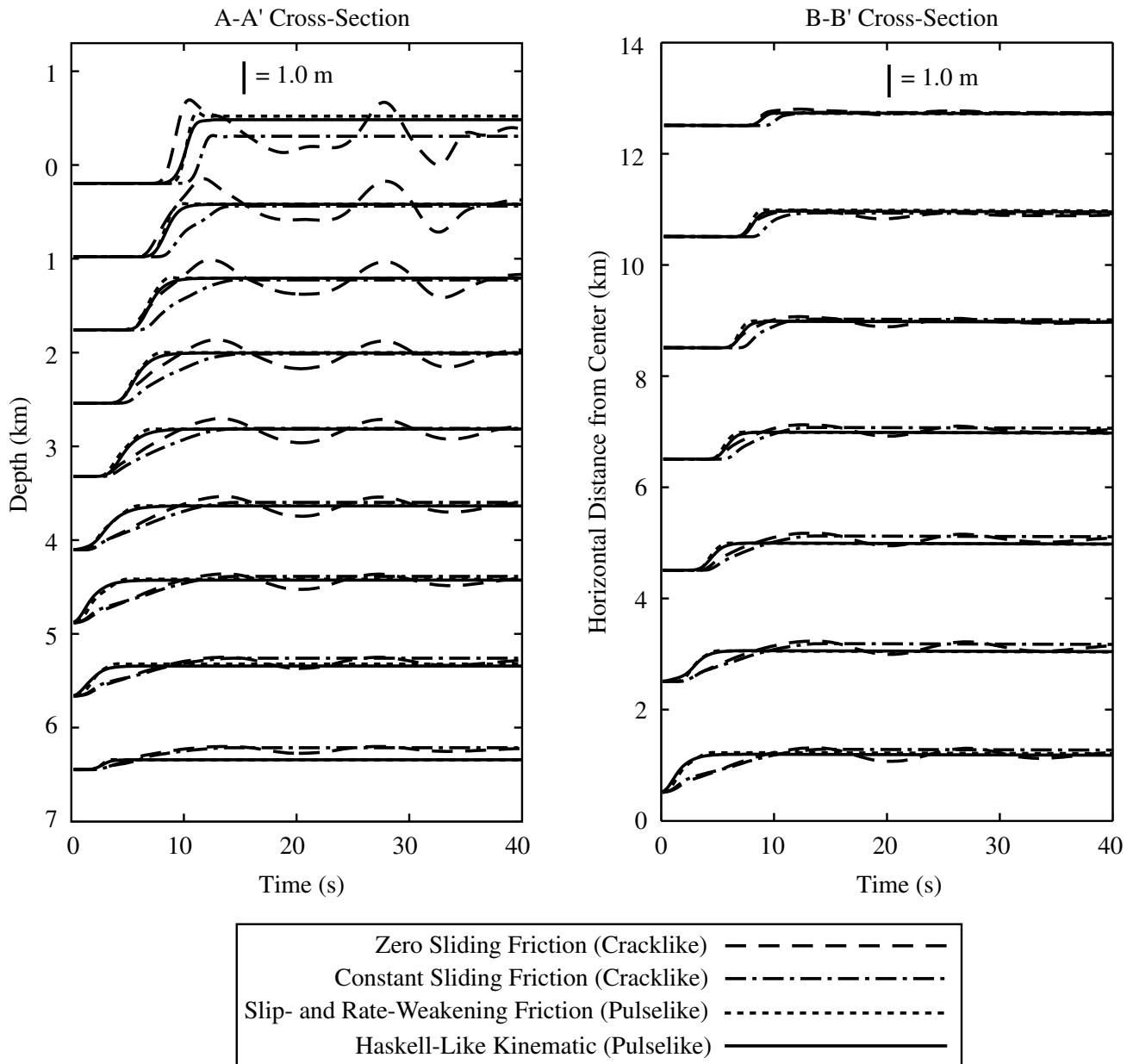


Figure 10. Slip histories are plotted for a series of grid points along AA' and BB'. Only the slip component perpendicular to strike is shown because any slip parallel to strike is minimal for points along the cross sections. There is approximately uniform slip with depth. Slip does increase some as the rupture approaches the free surface. Zero sliding friction's slip history oscillates about equilibrium with a period of 12 sec and radiation damping of 6%. The cracklike models, zero sliding friction and constant sliding friction, have long slip durations (up to 14 sec), and the pulselike models, slip- and rate-weakening friction and Haskell-like traditional kinematic rupture, have shorter slip durations (less than 5 sec). Therefore, the cracklike models allow more interactions between the rupture and radiated energy than the pulselike models.

we create synthetic seismograms of teleseismic P and SH body waves for a range of epicentral distances, $30^\circ < \Delta < 90^\circ$, and azimuths. The dynamic rupture-displacement jump time histories have been mapped into a regular grid of point-dislocation time histories, 18×28 points. The top row of points occurs 0.5 km down-dip from the free surface so there

are no point dislocations exactly at the free surface. All other boundary conditions (the Earth's free surface, displacements going to zero amplitude at infinite distances, material layering) are matched between the elastic continua and the dynamic ruptures. Resultant teleseismic P and SH body waves are calculated by using the method of Yao and Ji (1997) and

Yao and Harkrider (1983) that computes the response of a layered Earth to each point dislocation with $T_p^* = 1$ sec and $T_s^* = 4$ sec, for the attenuation. Note $T^* =$ travel time/quality factor (Q) and the amplitudes of the telesismic body waves are attenuated by the following relationship: $A = A_0 e^{-\pi f T^*}$, where f is frequency (Lay and Wallace, 1995, section 3.7). The earth structure through which the waves are propagated is iasp91 (Kennett and Engdahl, 1991), a radially stratified Earth model.

A test of whether wave-slip interactions produce sufficient fault opacity to affect the telesismic signal is to compare the telesismic peak-to-peak displacement amplitudes of the different ruptures; namely, if opacity is created by wave-slip interactions (reslipping), then one might expect that the dynamic rupture that allows the most wave-slip interactions should have the smallest peak-to-peak amplitudes, and the dynamic rupture that allows the least wave-slip interactions (transparent) should have the largest peak-to-peak amplitudes. If there is no trend, then the fault is not significantly opaque to telesismic radiation.

Synthetic Telesismic Seismogram Results

To examine how sources from different depths affect the solution, we plot P and SH telesismic displacements (Fig. 11) for a surface station at an azimuth of 45° and $\Delta = 60^\circ$. We first integrate the point time histories along-strike and plot the resultant displacement seismograms. These are shown with respect to depth in the top half of Figure 11. This intermediate result illustrates the depth dependence of the solution. We then integrate the time histories along-dip (second spatial dimension), to produce the telesismic P and SH displacement seismograms in the bottom half of Figure 11. These seismograms represent the solution for the entire fault.

Inspecting Figure 11, we see that zero sliding friction produces the seismograms with the largest peak-to-peak displacement amplitudes. As expected, at telesismic distances, the pulselike ruptures, slip- and rate-weakening friction, and Haskell-like traditional kinematic ruptures have similar waveforms. However, the two cracklike ruptures (zero sliding friction and constant sliding friction) are quite dissimilar, especially for sources near the surface, but approach the same shape (overlooking any time delays or subsequent oscillations about zero) for sources at depth. Note that near the surface, the pulselike ruptures have larger peak-to-peak displacement amplitudes than the cracklike constant sliding friction rupture, and at depth, the pulselike ruptures have smaller peak-to-peak displacement amplitudes than either cracklike rupture. This phenomenon is simply a result of the cracklike and pulselike ruptures partitioning their slip differently as a function of depth (Fig. 10).

In Figure 12, we explore the radiation pattern of the P and SH body waves by plotting the telesismic displacement time histories for surface receivers at different azimuths. We

compute the response for azimuths every 15° for 13 epicentral distances within the range, $30^\circ < \Delta < 90^\circ$; however, Figure 12 shows the results for only $\Delta = 60^\circ$ and azimuths 30° apart. A 30° separation gives a sufficient representation of the azimuthal variation, and different distances simply change the overall amplitude, not the shape of the waveform. In Table 3, we use all these computed azimuths for compiling the statistics.

One of the most important observations from Figure 12 is that constant sliding friction, slip- and rate-weakening friction, and Haskell-like traditional kinematic ruptures all have nearly identical waveforms at any particular azimuth. The cracklike constant sliding friction does have a time delay relative to the two pulselike ruptures of approximately 2.0–3.1 sec for P waves and 2.5–3.1 sec for SH waves; this is a consequence of the cracklike constant sliding friction rupture requiring a much longer period to complete its total slip than the pulselike rupture (Fig. 10). The similar waveforms for these ruptures indicate the seismograms are primarily controlled by rupture geometry, earthquake size, and rupture speed.

The quantified results in Table 3 provide additional insight. We compare the peak-to-peak displacement amplitudes of the three dynamic ruptures. Their amplitudes are normalized by the peak-to-peak displacement amplitudes of the Haskell-like traditional kinematic rupture to produce dimensionless numbers. The normalized peak-to-peak displacement amplitudes are averaged over azimuth for each epicentral distance and then averaged over distance. If the assumption that a transparent fault in Haskell-like dislocation theory leads to underestimates of seismic moment is correct, then the dynamic ruptures with the greatest wave-slip interactions would produce the smallest telesismic peak-to-peak displacement amplitudes. Furthermore, all the dynamic ruptures would have normalized numbers less than one.

Table 3 shows that the dynamic ruptures with wave-slip interactions do not have numbers noticeably less than one when normalized by the transparent, Haskell-like traditional kinematic rupture. Within approximately one standard deviation, all the numbers are either one or greater than one. Specifically, constant sliding friction has average values of 0.96 for P waves and 1.02 for SH waves, and slip- and rate-weakening friction has average values of 1.08 for P waves and 1.05 for SH waves. When the friction model is taken to the extreme case to produce the greatest fault wave-slip interactions, that is, zero sliding friction, the normalized peak-to-peak displacement amplitudes are considerably greater than one (1.65 for P waves and 2.03 for SH waves), just the opposite of what we would expect if wave-slip interactions produced opacity. In the next section, we demonstrate that these increased values are a result of the traction-free sliding surface, not opacity.

Hence, (1) there is no noticeable opacity, and (2) the wave-slip interactions fail to trap a sufficient fraction of en-

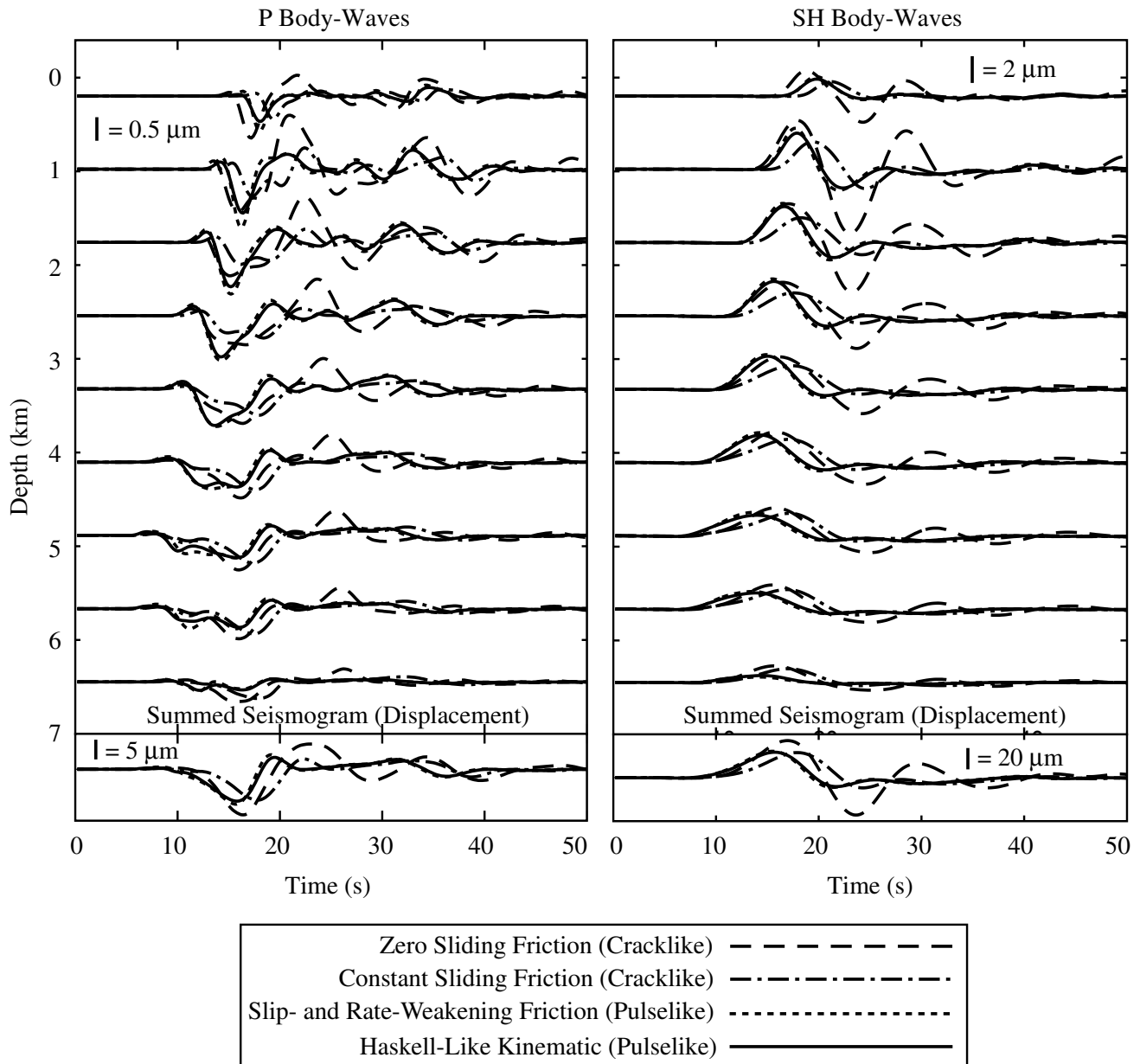


Figure 11. Synthetic seismograms for P body waves and SH body waves at an azimuth of 45° and $\Delta = 60^\circ$. The top portion shows the teleseismic response for point sources integrated along-strike at each depth. The bottom portion shows response for the entire fault rupturing, that is, integrated along-strike and along-dip. Zero sliding friction produces the largest peak-to-peak displacement amplitudes. The two pulse-like ruptures, slip- and rate-weakening friction and Haskell-like traditional kinematic rupture, have similar waveforms. The two cracklike ruptures, zero sliding friction and constant sliding friction, converge at depth. All the ruptures, except zero sliding friction, have similar waveforms for the entire fault rupturing in the bottom box. Constant sliding friction, however, has a time delay because it requires more time to complete its slip.

ergy in the hanging wall to reduce the amplitude of the teleseismic ground motions. This indicates that Haskell-like dislocation theory, with the assumption of a transparent fault, will not lead to underestimates of seismic moment.

Discussion

Peak-to-Peak Displacement Amplitudes

The peak-to-peak displacement amplitudes we use to measure the size of teleseismic ground motion have the fol-

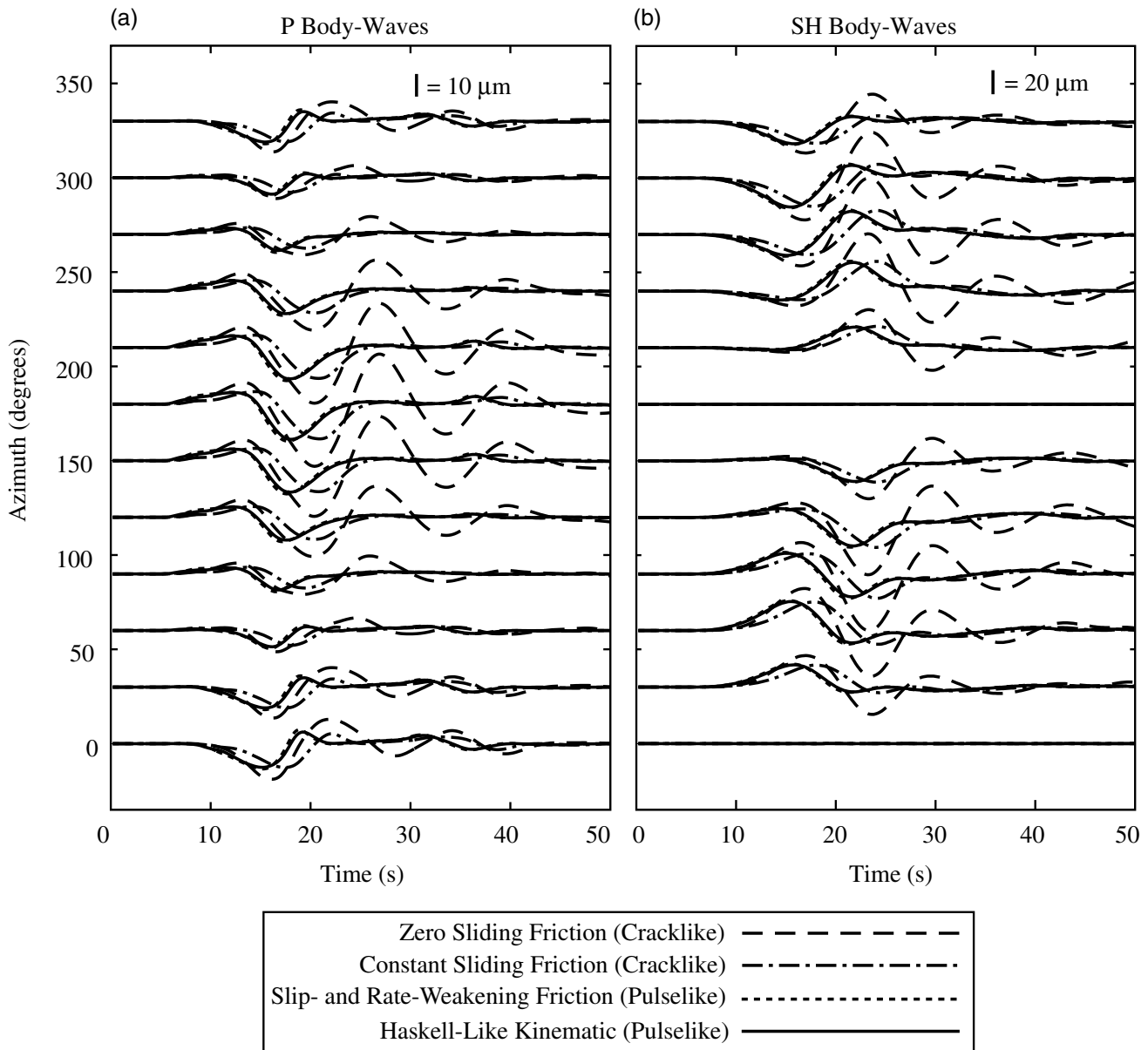


Figure 12. Synthetic seismograms for (a) *P* body waves and (b) *SH* body waves at $\Delta = 60^\circ$ for azimuths 30° apart to display the radiation patterns. Constant sliding friction, slip- and rate-weakening friction, and Haskell-like traditional kinematic rupture all have nearly identical waveforms at any particular azimuth. The only significant difference is that constant sliding friction has a time delay because it requires more time to complete its slip. This similarity indicates that rupture geometry, earthquake size, and rupture speed, not degree of wave-slip interactions, are primarily determining the waveform shapes and sizes. When wave-slip interactions are taken to the extreme (zero sliding friction), larger, not smaller, peak-to-peak displacement amplitudes are generated. This is due to an effect other than opacity (see Discussion and Fig. 15).

lowing correspondence to seismic phases and crustal reverberations. By comparing seismograms in Figure 12 for the *P* body waves with those in Figure 13 (Green's functions for impulsive point sources), one can see that the small initial positive peak at about 14–15 sec for azimuths 90° – 270° comes from the *P* phase, which is largest at azimuth 180° and has a significant signal for the 90° on either side. A

substantial negative peak occurs later in time, anywhere from 15 to 21 sec, for all azimuths. This is due to a combined effect of *pP* and *sP*. For the plotted azimuths 0° – 90° and 270° – 330° , *pP* is the primary phase contributing to the negative signal, and for azimuths 120° – 240° , *sP* is the primary phase contributing to the negative signal. Because *sP* arrives later than *pP* and the *sP* becomes increasingly dominant as a sta-

Table 3
Averaging the Dynamic Models' Peak-to-Peak Displacement Amplitudes in P and SH over Azimuth and Normalizing by the Transparent, Haskell-like Traditional Kinematic Model

Epicentral Distance, Δ	Zero Sliding Friction		Constant Sliding Friction		Slip- and Rate-Weakening Friction	
	Peak-to-Peak Averaged over Azimuth	Stand. Dev. (%)	Peak-to-Peak Averaged over Azimuth	Stand. Dev. (%)	Peak-to-Peak Averaged over Azimuth	Stand. Dev. (%)
a. P body waves						
31°	1.71	10.5	0.97	4.9	1.07	2.6
45°	1.69	9.6	0.97	4.6	1.08	3.0
60°	1.65	9.4	0.96	4.6	1.08	3.3
75°	1.61	9.9	0.95	4.9	1.09	3.8
89°	1.55	12.1	0.93	4.6	1.10	4.2
Averaged over Δ	1.65		0.96		1.08	
b. SH body waves						
31°	2.04	8.2	1.02	1.2	1.05	0.7
45°	2.04	7.5	1.02	0.9	1.05	0.6
60°	2.03	6.4	1.02	0.9	1.05	0.4
75°	2.03	5.1	1.02	0.8	1.05	0.2
89°	2.02	4.0	1.02	0.7	1.05	0.1
Averaged over Δ	2.03		1.02		1.05	

Numbers <1 indicate the transparent fault assumption underestimates the moment. Numbers >1 indicate the transparent fault assumption overestimates the moment. Numbers approximately 1 indicate the transparent fault assumption has no effect on the moment estimate. (a) Statistics for P body waves. (b) Statistics for SH body waves.

tion is moved closer to an azimuth of 180° , the negative peak shifts later and later in time the closer a station is to an azimuth of 180° . For azimuths $0-60^\circ$ and $310-330^\circ$, one can see a small positive peak at 18–22 sec (depending on the model), that follows the first negative peak. It is due to a small positive sP at those azimuths and crustal reverberations within the material layers.

Examining the SH body waves in Figure 12 and the Green's functions in Figure 14, the initial positive peak for azimuths $30-150^\circ$ and initial negative peak for azimuths $210-330^\circ$ which occur at 15–18 sec, are simply due to the direct S seismic phase. Then for slightly later times, 22–24 sec, a negative peak follows the positive one for azimuths $30-150^\circ$, and a positive peak follows the negative one for azimuths $210-330^\circ$. This is due to a combined effect of sS and crustal reverberations. For azimuths $90-150^\circ$ and $210-270^\circ$, sS is the larger wave, whereas crustal reverberations are the larger waves for the other azimuths.

Wave-Slip Interactions (Reslipping)

We have shown that the long-slip-duration cracklike models, zero sliding friction and constant sliding friction, would have the most opportunity for wave-slip interactions that produce reslipping (where radiated waves cause the fault to reslip, producing a partially opaque fault boundary). The pulselike model, slip- and rate-weakening model, is less likely to see significant wave-slip interactions (opacity) because of its shorter slip durations. We have also shown that whatever wave-slip interaction exists, it has a small effect

on the teleseismic peak-to-peak displacement amplitudes, except in zero sliding friction.

It is difficult to separate explicitly the effects of wave-slip interaction between the rupture and reflected phases from other dynamic effects. The important point is that we generate ruptures that allow differing levels of wave-slip interactions. Thus, this study focuses on whether Haskell-like dislocation theory, which assumes a transparent fault boundary, is an adequate description of the rupture process for teleseismic signals generated by ruptures on a shallow-dipping thrust fault where significant wave-slip interactions may occur. Accordingly, our results indicate that Haskell-like dislocation modeling is indeed adequate.

The zero sliding friction dynamic rupture produces teleseismic peak-to-peak displacement amplitudes considerably larger than the other three ruptures, approximately 60% larger in P and 100% larger in SH . This difference in peak-to-peak displacement amplitudes is caused by dynamic effects associated with the oscillations. Figure 15 shows the potency rate of the different ruptures as a function of time. The Fourier amplitude spectrum of the potency rate is also shown. Notice that the zero sliding friction rupture has the same spectral amplitude as the other three ruptures for zero frequency (this value is determined by the final potency) but has a much larger spectral amplitude than any other rupture for 0.06–0.18 Hz with a peak at 0.08 Hz. This peak corresponds to the slip oscillation period of 12 sec. The peak-to-peak displacement amplitudes measured for zero sliding friction in Table 3 are associated with this nonzero frequency, which is why we obtain normalized numbers much larger

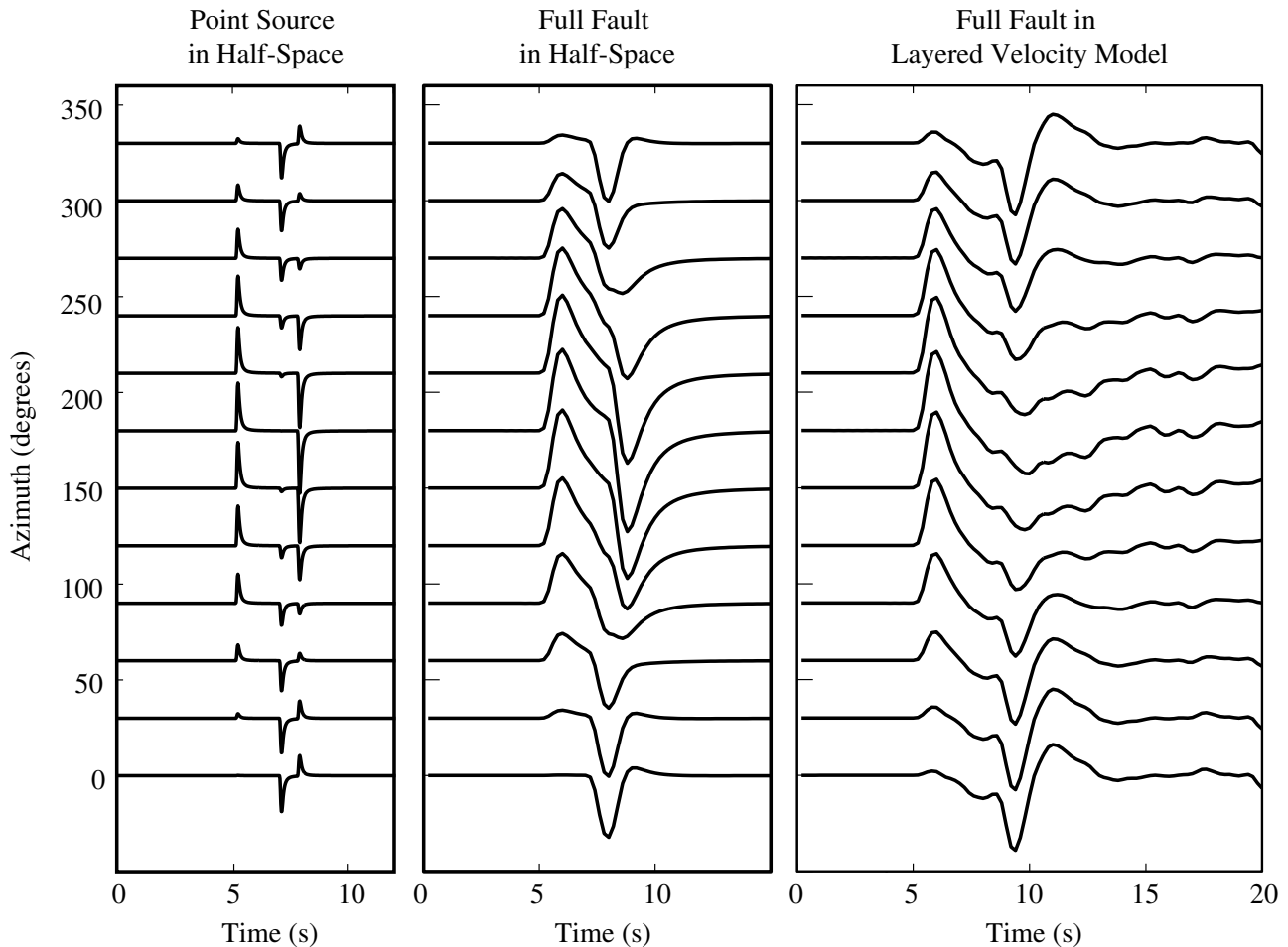


Figure 13. The dip-slip component of the Green's functions for the P waves. Because the rake is almost exactly 90° in our simulations, dip-slip is the appropriate component to study to understand the effect of reflected phases in our seismograms. On the left is the Green's function for an impulsive point source at approximately 6.5 km depth in a half-space. Note that for the point source, Q is increased to reduce the attenuation; this clearly delineates the three main phases, P , pP , and sP . Q is increased by reducing t^{*P} from 1.0 sec to 0.1 sec. In the center panel, the sum of the Green's functions for the entire fault rupturing in a half-space is plotted. In this case $t^{*P} = 1.0$ sec, but it has little effect because the summation of the point sources also filters out the high-frequency information. Notice in this center panel that the effects of P , pP , and sP merge together. The panel on the right shows the summed Green's functions for the entire fault rupturing through the velocity model we use in the simulations. It shows how material layering and associated crustal reverberations alter the signal.

than those for any other rupture. The oscillations with a spectral peak of 0.08 Hz are a result of the unrealistic friction model (sliding friction of zero), and they demonstrate the substantial difference in behavior between zero sliding friction and the other ruptures.

Mode I Opening

Brune's (1996) foam-rubber block experiments and our dynamic rupture simulations have dramatically different mode I behaviors. Specifically, the foam-rubber experiments experience significant mode I opening; whereas our dynamic

ruptures slip only in the mode II and mode III directions. Restricting slip to mode II and mode III is a valid assumption, because when we allow mode I opening, we find it has a negligible effect. Permitting mode I opening produces slips, displacements, and velocities that are indistinguishable from the case of preventing mode I opening, except close to the free surface where there are some minute differences. In addition, it produces indistinguishable teleseismic displacements. Because we are interested only in teleseismic signals, far away from the surface trace, including mode I opening is not important.

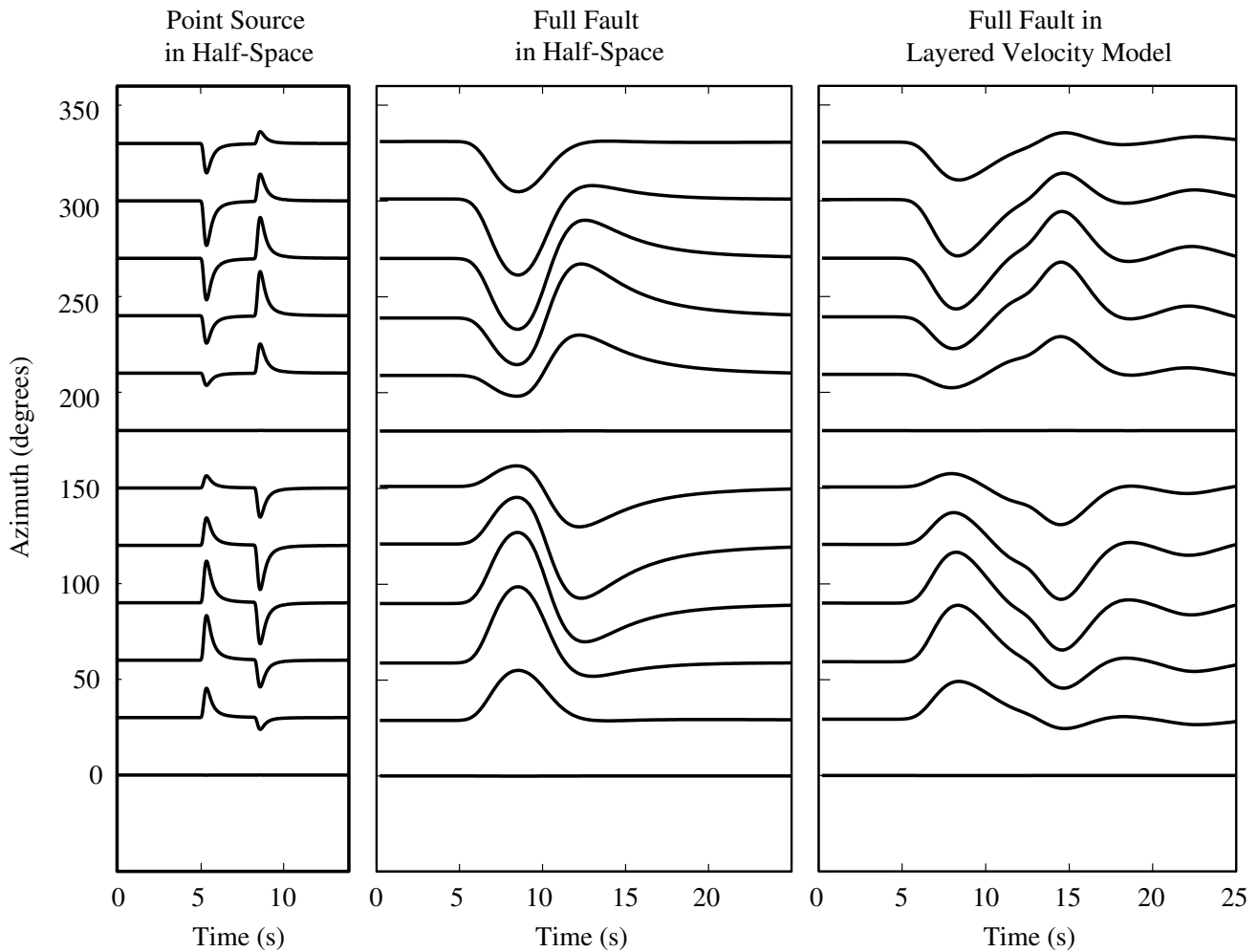


Figure 14. The dip-slip component of the Green's functions for the SH waves. On the left is the Green's function for an impulsive point source at approximately 6.5 km depth in a half-space. Note that for the point source, Q is increased to reduce the attenuation; this clearly delineates the two main phases, S and sS . Q is increased by reducing t^{*S} from 4.0 sec to 0.4 sec. In the center panel, the sum of the Green's functions for the entire fault rupturing in a half-space is plotted. In this case $t^{*S} = 4.0$ sec, but it has little effect because the summation of the point sources also filters out the high-frequency information. Notice in this center panel that the effects of S and sS merge. The panel on the right shows the summed Green's functions for the entire fault rupturing through the velocity model we use in the simulations. It shows how material layering and associated crustal reverberations alter the signal.

The primary reason we do not see significant mode I opening in our dynamic ruptures is that the overburden pressure caused by gravity keeps the fault closed (except as the rupture breaks the Earth's surface). In the foam-rubber experiments, the fault normal stress and shear stress are approximately equal, whereas in our simulations the normal pressure is approximately 10 to 20 times greater than the effective shear stress (true shear stress minus sliding frictional traction) at seismogenic depths. This indicates that the foam-rubber results are primarily representative of the shallow surface. A 2D lattice model study has also observed mode I opening over a significant percentage of the fault (Shi *et al.*, 1998). Although many of the parameters are more

representative of the Earth than foam-rubber block models, based on the amount of slip relative to the model size, these simulations appear to be applicable to depths of less than 1 km. We come to this order-of-magnitude estimate as follows: (1) Assume that the total displacement is about 1 m, (2) notice that the total displacement in the simulation is about one grid cell length (therefore, one grid cell is approximately equivalent to 1 m), and (3) then use this to scale the simulation of 256 by 256-grid cells. This leads to a maximum fault length of 256 m, indicating this simulation has tested only the shallow-fault cause. Thus, it seems that small overburden pressures permit fault opening in the foam-rubber and 2D lattice models, whereas larger overburden

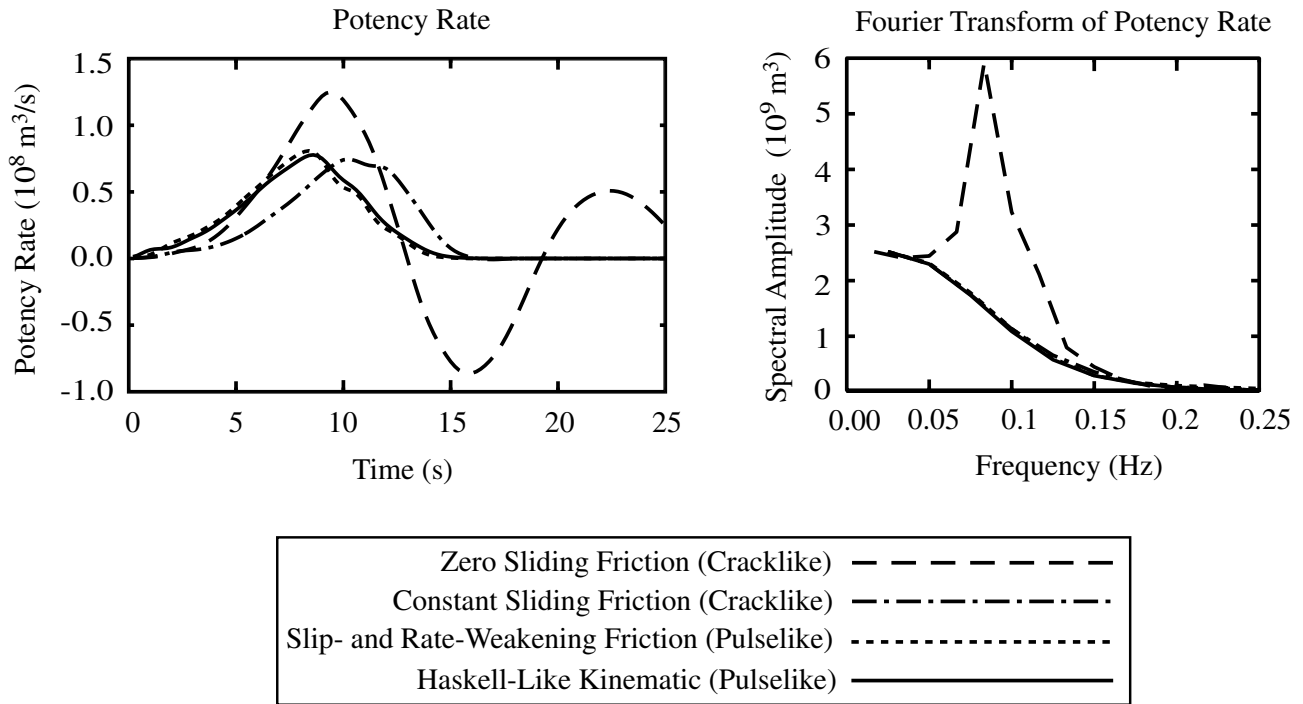


Figure 15. Potency rate for the entire fault rupturing (left) and the Fourier transform of this potency rate, that is, the spectral amplitude (right). Note that the zero sliding friction has a spectral amplitude peak at 0.08 Hz, which coincides with the oscillation period of 12 sec that is seen in the slip histories.

pressures appropriate for seismogenic depths, suppress this type of fault behavior.

There is one source of mode I opening, Weertman waves, that we are unable to test because of the length scale of our numerical simulations. Weertman waves are wrinkle-like slip pulses produced in ruptures where there is a contrast in material properties across the slip plane (Weertman, 1980; Andrews and Ben-Zion, 1997; Cochard and Rice, 2000). However, including Weertman waves should create little or no opportunity for opacity in our dynamic ruptures because Weertman waves are a short-length-scale phenomenon. That is, only a small portion of the fault, directly behind the rupture front, would be opaque at any instant. Although it remains to be shown what length scale is needed to make faults opaque to teleseismic radiation, it would be longer than what is permitted by physics as we understand it.

On the other hand, a rupture with disparate material properties on either side of the fault could experience other effects that would change the teleseismic signals and slip estimates. Several articles have discussed how the local dynamics change (Andrews and Ben-Zion, 1997; Harris and Day, 1997; Rubin and Gillard, 2000; Ranjith and Rice, 2001; Ben-Zion and Huang, 2002), but we have yet to study how it affects teleseismic ground motions. This is an important issue because subduction zones, which account for most of the total earthquake moment on the Earth, typically have a strong material property contrast across their faults.

Conclusion

Brune (1996) suggested that earthquakes experience wave-slip interactions that produce opaque fault ruptures. Therefore, we asked, can Haskell-like dislocation models of earthquakes in which a transparent fault boundary is assumed, lead to underestimates of the seismic moments of shallow-dipping thrust fault events? Using 3D dynamic rupture simulations for faults with varying levels of wave-slip interactions, we numerically test this question and find no evidence for opacity. We compare the teleseismic ground motions of dynamic ruptures (with varying levels of wave-slip interactions in an attempt to produce fault boundary opacity) and a Haskell-like traditional kinematic reference rupture (there are no wave-slip interactions; therefore, it has a transparent fault boundary). If wave-slip interactions produce significant opacity to teleseismic waves, the models with greater wave-slip interactions would produce smaller peak-to-peak displacement amplitudes (which would lead to smaller moment estimates). Instead, we find that peak-to-peak displacement amplitudes of teleseismic *P* and *SH* body waves are not affected by the level of wave-slip interactions. In the unrealistic case of zero sliding friction, we see a difference in the peak-to-peak displacement amplitudes, but this is due to an effect other than wave-slip interactions trapping energy in the hanging wall of the fault. Specifically, the oscillatory behavior of the zero sliding friction creates far-field seismic radiation that increases the peak-to-peak

displacement teleseismic amplitudes relative to the other models. In the frequency domain (Fig. 15), we see that it has the same potency or zero frequency energy as the other models, but zero sliding friction has a nonzero frequency spectral peak associated with the far-field radiation. Consequently, opacity is not significant for teleseismic motion calculations; it is fine to assume a transparent fault boundary when using dislocation modeling for teleseismic data.

Our results should not be surprising given that Wald and Heaton (1994), Wald *et al.* (1996), and Ji *et al.* (2002, 2003) have shown it is possible to approximately match near-source seismograms, geodetic data, and teleseismic seismograms simultaneously with the same finite-source models. Because the models fit each of the different data sets simultaneously, this suggests that the current use of dislocation models can adequately represent the source. Furthermore, because the dislocation model can be used to determine radiated energy uniquely (Aagaard *et al.*, 2001), there should be no inconsistency in the radiated energy from the different data sets. Indeed, the reported discrepancy between near-source and teleseismic estimates of radiated energy is now being resolved through refinements of energy estimate techniques for strike-slip faults (Boatwright *et al.*, 2002) and may be resolved for dip-slip faults as well.

Acknowledgments

This material is based on work supported by National Science Foundation Grant 0208494. We thank Chen Ji for modifying his code so we could forward-model teleseismic ground motions for any given slip history. We also thank James Brune, Pascal Favreau, Ruth Harris, Art McGarr, and David Oglesby for their insightful and helpful reviews and Barbara Smith for her editing. Access to the Hewlett-Packard V-Class computer, located at the California Institute of Technology, was provided by the Center for Advance Computing Research.

References

- Aagaard, B. T. (1999). Finite-element simulations of earthquakes, Technical Report No. 99-03, California Institute of Technology, Earthquake Engineering Research Laboratory, Pasadena, California.
- Aagaard, B. T., J. F. Hall, and T. H. Heaton (2001). Characterization of near-source ground motions with earthquake simulations, *Earthquake Spectra* **17**, 177–207.
- Achenbach, J. D. (1973). *Wave Propagation in Elastic Solids*, American Elsevier Publishing Company, New York, 425 pp.
- Andrews, D. (1976a). Rupture propagation with finite stress in antiplane strain, *J. Geophys. Res. Solid Earth* **81**, 3575–3582.
- Andrews, D. (1976b). Rupture velocity of plane strain shear cracks, *J. Geophys. Res.* **81**, 5679–5687.
- Andrews, D. J., and Y. Ben-Zion (1997). Wrinkle-like slip pulse on a fault between different materials, *J. Geophys. Res. Solid Earth* **102**, 553–571.
- Ben-Zion, Y., and Y. Q. Huang (2002). Dynamic rupture on an interface between a compliant fault zone layer and a stiffer surrounding solid, *J. Geophys. Res. Solid Earth* **107**, 2042, doi 10.1029/2001JB000254.
- Ben-Zion, Y., and L. Zhu (2002). Potency-magnitude scaling relations for southern California earthquakes with $1.0 < M-L < 7.0$, *Geophys. J. Int.* **148**, F1–F5.
- Boatwright, J., G. L. Choy, and L. C. Seekins (2002). Regional estimates of radiated seismic energy, *Bull. Seism. Soc. Am.* **92**, 1241–1255.
- Brune, J. N. (1970). Tectonic stress and the spectra of seismic shear waves from earthquakes, *J. Geophys. Res. Solid Earth* **75**, 4997–5009.
- Brune, J. N. (1996). Particle motions in a physical model of shallow angle thrust faulting, *Proc. Indian Acad. Sci. Earth Planet. Sci.* **105**, L197–L206.
- Burridge, R., G. Conn, and L. Freund (1979). The stability of rapid mode II shear crack with finite cohesive traction, *J. Geophys. Res. Solid Earth* **85**, 2210–2222.
- Cochard, A., and J. R. Rice (2000). Fault rupture between dissimilar materials: Illposedness, regularization, and slip-pulse response, *J. Geophys. Res. Solid Earth* **105**, 25,891–25,907.
- Day, S. M. (1982). Three-dimensional simulation of spontaneous rupture: the effect of nonuniform prestress, *Bull. Seism. Soc. Am.* **72**, 1881–1902.
- Harris, R. A., and S. M. Day (1997). Effects of a low-velocity zone on a dynamic rupture, *Bull. Seism. Soc. Am.* **87**, 1267–1280.
- Haskell, N. A. (1964). Total energy and energy spectral density of elastic wave radiation from propagating faults, *Bull. Seism. Soc. Am.* **54**, 1811–1841.
- Heaton, T. H. (1990). Evidence for and implications of self-healing pulses of slip in earthquake rupture, *Phys. Earth Planet. Interiors* **64**, 1–20.
- Heaton, T. H., and R. E. Heaton (1989). Static deformations from point forces and forces couples located in welded elastic poissonian half-spaces: implications for seismic moment tensors, *Bull. Seism. Soc. Am.* **79**, 813–841.
- Ida, Y. (1972). Cohesive force across the tip of a longitudinal-shear crack and Griffith's specific surface energy, *J. Geophys. Res. Solid Earth* **77**, 3796–3805.
- Ji, C., D. V. Helmberger, D. J. Wald, and K. F. Ma (2003). Slip history and dynamic implications of the 1999 Chi-Chi, Taiwan, earthquake, *J. Geophys. Res. Solid Earth* **108**, 2412, doi 10.1029/2002JB001764.
- Ji, C., D. J. Wald, and D. V. Helmberger (2002). Source description of the 1999 Hector Mine, California earthquake. Part II: Complexity of slip history, *Bull. Seism. Soc. Am.* **92**, 1208–1226.
- Kennett, B. L. N., and E. R. Engdahl (1991). Traveltimes for global earthquake location and phase identification, *Geophys. J. Int.* **105**, 429–465.
- Lay, T., and T. C. Wallace (1995). *Modern Global Seismology* Academic Press, San Diego, 521 pp.
- Madariaga, R. (2003). Radiation from a finite reverse fault in a half space, *Pure Appl. Geophys.* **160**, 555–577.
- Madariaga, R., and A. Cochard (1996). Dynamic friction and the origin of the complexity of earthquake sources, *Proc. Natl. Acad. Sci.* **93**, 3819–3824.
- Madariaga, R., K. Olsen, and R. Archuleta (1998). Modeling dynamic rupture in a 3D earthquake fault model, *Bull. Seism. Soc. Am.* **88**, 1182–1197.
- Mansinha, L., and D. E. Smylie (1971). The displacement fields of inclined faults, *Bull. Seism. Soc. Am.* **61**, 1433–1440.
- Okada, Y. (1992). Internal deformation due to shear and tensile faults in a half-space, *Bull. Seism. Soc. Am.* **82**, 1018–1040.
- Parsons, I., J. Hall, and G. Lyzenga (1988). Relationships between the average offset and the stress drop for two-dimensional and three-dimensional faults, *Bull. Seism. Soc. Am.* **78**, 931–945.
- Ranjith, K., and J. R. Rice (2001). Slip dynamics at an interface between dissimilar materials, *J. Mech. Phys. Solids* **49**, 341–361.
- Rubin, A. M., and D. Gillard (2000). Aftershock asymmetry/rupture directivity among central San Andreas fault microearthquakes, *J. Geophys. Res. Solid Earth* **105**, 19,095–19,109.
- Shi, B., A. Anooshehpour, J. N. Brune, and Y. Zeng (1998). Dynamics of thrust faulting: 2D lattice model, *Bull. Seism. Soc. Am.* **88**, 1484–1494.
- Shoja-Taheri, J., and J. G. Anderson (1988). The 1978 Tabas, Iran, earthquake: an interpretation of the strong motion records, *Bull. Seism. Soc. Am.* **78**, 142–171.
- Sing, S. K., and M. Ordaz (1994). Seismic energy release in Mexican subduction zone earthquakes, *Bull. Seism. Soc. Am.* **84**, 1533–1550.

- Somerville, P., K. Irikura, R. Graves, S. Sawada, D. Wald, N. Abrahamson, Y. Iwasaki, T. Kagawa, N. Smith, and A. Kowada (1999). Characterizing crustal earthquake slip models for the prediction of strong ground motion, *Seism. Res. Lett.* **70**, 59–80.
- Wald, D. J., and T. H. Heaton (1994). Spatial and temporal distribution of slip for the 1992 Landers, California, earthquake, *Bull. Seism. Soc. Am.* **84**, 668–691.
- Wald, D. J., T. H. Heaton, and K. W. Hudnut (1996). The slip history of the 1994 Northridge, California, earthquake determined from strong-motion, teleseismics, GPS, and leveling data, *Bull. Seism. Soc. Am.* **86**, (Part B Supplement S), S49–S70.
- Weertman, J. (1980). Unstable slippage across a fault that separates elastic media of different elastic-constants, *J. Geophys. Res.* **85**, 1455–1461.
- Yao, Z. X., and D. G. Harkrider (1983). A generalized reflection-transmission coefficient matrix and discrete wavenumber method for synthetic seismograms, *Bull. Seism. Soc. Am.* **73**, 1685–1699.
- Yao, Z.-X., and C. Ji (1997). The inverse problem of finite fault study in time domain, *Chinese J. Geophys.* **40**, 691–701.

Department of Geology and Planetary Science
MS 252-21
CALTECH
Pasadena, California 91125
(D.E.S., T.H.H.)

U.S. Geological Survey
MS 977
345 Middlefield Road
Menlo Park, California 94025
(B.T.A.)

Manuscript received 15 August 2003.